energies

MDPI

Article

Inertia Estimation of Regional Power Systems Using Band-Pass Filtering of PMU Ambient Data

Kyeong-Yeong Lee [1], Sung-Guk Yoon [1,2,*] and Jin Kwon Hwang [3,*]

[1] Department of Convergence of Energy Policy and Technology, Soongsil University, Seoul 06978, Republic of Korea; elecky@soongsil.ac.kr
[2] Department of Electrical Engineering, Soongsil University, Seoul 06978, Republic of Korea
[3] Department of Energy and Electrical Engineering, Woosuk University, Jinchon-gun 27814, Republic of Korea
* Correspondence: sgyoon@ssu.ac.kr (S.-G.Y.); jkhwangdm@yahoo.com (J.K.H.)

Abstract

This paper proposes a regional inertia estimation method in power systems using ambient data measured by phasor measurement units (PMUs). The proposed method employs band-pass filtering to suppress the low-frequency influence of mechanical power and to attenuate high-frequency noise and discrepancies between rotor speed and electrical frequency. By utilizing a simple first-order AutoRegressive Moving Average with eXogenous input (ARMAX) model, this process allows the inertia constant to be directly identified. This method requires no prior model order selection, rotor speed estimation, or computation of the rate of change of frequency (RoCoF). The proposed method was validated through simulation on three benchmark systems: the Kundur two-area system, the IEEE Australian simplified 14-generator system, and the IEEE 39-bus system. The method achieved area-level inertia estimates within approximately ±5% error across all test cases, exhibiting consistent performance despite variations in disturbance models and system configurations. The estimation also maintained stable performance with short data windows of a few minutes, demonstrating its suitability for near real-time monitoring applications.

Keywords: ARMAX model; band-pass filtering; PMU ambient data; regional inertia estimation

1. Introduction

In conventional power systems, inertia refers to the rotational energy stored in their rotor masses and turbine shafts [1]. This inertia plays a critical role in maintaining the balance between power supply and demand, as it can momentarily absorb or release energy to mitigate frequency fluctuations in the power system. In recent years, the increasing integration of renewable energy sources has accelerated the shift in power systems from conventional synchronous generators (SGs) to converter-interfaced generators (CIGs) [2]. Unlike traditional rotor-based machines, CIGs do not contain any physical rotating machinery, thereby reducing the natural system inertia. The reduced inertia significantly increases the rate of change of frequency (RoCoF) following disturbances, which curtails the time available for control actions and poses serious challenges to maintaining frequency stability in power system operations [3]. As future power systems become increasingly low-inertia, continuous monitoring of inertia will be essential to ensure reliable system operation [4]. In power system operation, such low-inertia conditions have already been observed in systems with a high penetration of photovoltaic generation, where relatively small power imbalances can trigger fast frequency deviations and elevated RoCoF. Recent studies on

Check for updates

Academic Editors: Zbigniew Hanzelka, Ryszard Sroka, Ryszard Klempka and Jerzy Dzieża

Received: 28 November 2025
Revised: 28 December 2025
Accepted: 12 January 2026
Published: 15 January 2026

Copyright: © 2026 by the authors. Licensee MDPI, Basel, Switzerland. This article is an open access article distributed under the terms and conditions of the Creative Commons Attribution (CC BY) license.

large-scale microgrid environments have reported that, under real operating conditions with high photovoltaic penetration, reduced system inertia can lead to increased frequency deviations and elevated RoCoF [5].

Regional inertia estimation has attracted growing attention because system inertia is not uniformly distributed and can vary significantly across locations, especially in systems with a high penetration of converter-interfaced generators. Although system-wide inertia values provide a broad overview, they often fail to capture localized dynamic behaviors that influence protection schemes, frequency stability, and inverter-based resource control. Regional inertia monitoring, therefore, offers transmission system operators (TSOs) actionable information to maintain stability and respond effectively to local disturbances. Consequently, this research focuses on regional inertia estimation to address these critical challenges in modern power systems.

The literature on inertia estimation is categorized into ringdown data, probing signal data, and ambient data, depending on the type of data used [6–8]. Ringdown data captures transient conditions resulting from significant imbalances between power supply and demand, such as those caused by transmission line trips, generator failures, or huge load fluctuations [8]. Probing signal data includes responses to artificially injected input signals, allowing researchers to more precisely identify and analyze the dynamic characteristics of the system [9]. Ambient data, conversely, comprises the naturally occurring, stochastic fluctuations inherent to quasi-steady state operation. Although continuous, this data yields information that is less dynamically distinct than that obtained from controlled disturbances [10]. Given these data characteristics, both ringdown and probing signal data provide clearer insight into the dynamic behavior of the system. However, availability of ringdown data is often limited, and acquisition of probing data typically involves high experimental costs due to the need for specialized tests and facilities [11]. These limitations have led to a significant interest in the development of inertia estimation methods that employ readily available and low-cost ambient data. Recent studies have further demonstrated that ambient-data-based inertia estimation remains feasible and informative in low-inertia systems with high penetration of converter-interfaced generation. This includes applications in renewable-based microgrids operating under normal conditions [12]. In summary, the limited occurrence of ringdown events and the high experimental cost associated with probing-based approaches indicate that these data sources are not well suited for continuous inertia monitoring. From this perspective, the use of ambient data, which can be continuously acquired under normal operating conditions, becomes a natural and practical choice. Accordingly, this research focuses on inertia estimation using ambient data, taking into account the characteristics of such measurements.

In addition to the classification based on the data utilized, it is also possible to classify inertia estimation methods according to the underlying estimation principle. In [13], the effective real-time inertial monitoring has been enabled by identifying the system as a combined model of inertial response and primary frequency control through wide area ambient measurement during normal operation. In [11], an online estimation method for the inertial constant has been proposed, based on the identification of the state space model by the Numerical algorithm for Subspace State Space System IDentication (N4SID) method. In particular, the works in [11,13] are similar in that they derive the inertia constant from the RoCoF of the identified system frequency response. In [14], a method using the equation error system identification (SI) has been proposed for estimating the inertia constant. This method models the relationship between rotor internal frequency variation and active power variation with a transfer function that incorporates primary frequency control.

As an alternative to the SI method, an inertia estimation approach has been proposed based on mode information in [15,16]. In the first work, effective inertia was estimated

based on mode information derived from modal eigenvalues and mode shapes of vibrations occurring in different regions. In [16], inertia was estimated using the frequency, amplitude ratio, and synchronization power between the two divided regions. In [17,18], the estimated inertia was calculated using the statistical properties of colored noise in electrical quantities occurring as a result of load fluctuations. In [17], the system parameters and inertia were defined as functions, and then the equivalent inertia constant and damping coefficient were estimated by minimizing the nonlinear least squares cost function using the variance of the measured electrical quantity. Recently, probabilistic approaches based on Bayesian inference have been proposed to estimate inertia from ambient PMU measurements under normal operating conditions. These methods typically adopt dynamic models similar to those used in SI-based frameworks, while estimating inertia parameters through probabilistic inference that explicitly accounts for measurement noise and modeling uncertainty [19]. In parallel with these statistical approaches, deep learning-based methods have been introduced to directly learn the mapping between ambient measurement features and system inertia. For example, Convolutional Neural Networks (CNNs) have been employed to extract representative patterns from electrical measurement statistics and to estimate inertia without explicitly identifying a physical system model [18]. Also, advanced artificial intelligence-based frameworks have been proposed to extend such learning-based inertia estimation to renewable-dominated and inverter-based power systems, demonstrating their applicability to real-time inertia estimation under high penetration of converter-interfaced generation [20]. As such, various methods have been proposed for the estimation of inertia, and among them, SI is a widely used method [6] and is considered robust and accurate [21]. Therefore, this paper will focus on SI using ambient data.

However, there are limitations to applying SI methods using ambient data. First, determining the appropriate system order is challenging. In [11,13], an algorithm is proposed that identifies the system using Nth-order models ranging from $N = 1$ to 28 and then selects the order that best represents the system. However, since the inertia constant cannot be calculated directly from the identified model, the inertia constant is derived by converting the identified system to a continuous-time transfer function model via an impulse or step response and then estimating the RoCoF value again. During this conversion and estimation process, errors may occur in the estimation of the RoCoF. To estimate the inertia of an SG in [14], the system is identified by assuming a Second-order model. The inertia value is then calculated while considering the influence of the mechanical power P_m. In general, estimating the inertia of a power system poses several challenges. Since the transfer function of a CIG, which provides virtual inertia, is expressed in first order, determining the appropriate system order is required in regions where SGs and CIGs are mixed. Second, data pre-processing and practical applicability are considerable challenges. Typically, for inertia estimation by SI, the input is electrical power P_e and the output is rotor speed ω_r. Electrical frequency f is often used as a proxy for ω_r. However, the internal reactance of the SG causes the electrical frequency to differ from the actual rotor speed [22], making the approximation valid only at low frequencies [23]. In addition, commonly used low-pass filters for rotor speed estimation have cut-off frequencies around 0.5 to 1 Hz [11,23,24]. Under these conditions, it becomes increasingly difficult to effectively remove the influence of P_m, which cannot be directly measured by PMU [25]. Overall, these limitations highlight the challenges of model-order selection, preprocessing complexity, and indirect inertia estimation in SI-based approaches using ambient data.

Previous approaches often rely on higher-order models or explicit representations of P_m and governor dynamics, which increase model complexity and require careful system-order selection. In addition, inertia is frequently obtained indirectly through post-processing steps, such as RoCoF estimation, which may introduce additional sources

of error. Moreover, the common practice of using f as a proxy for ω_r is valid only within a limited low-frequency range, while typical filtering strategies further restrict the usable bandwidth and complicate the treatment of unmeasurable P_m variations. These limitations motivate the need for a simplified identification framework that can directly estimate inertia from ambient PMU measurements while reducing model-order ambiguity and preprocessing requirements.

Considering these limitations, this paper proposes a regional inertia estimation method in power systems by applying band-pass filtering to PMU ambient data within the SI with a model of the first order. The main contributions of this paper are as follows.

- The proposed method reformulates regional inertia estimation under ambient operating conditions as a first-order SI problem by applying band-pass filtering to PMU measurements. It is because, within the considered frequency band, mechanical power variations are sufficiently attenuated, and the terminal-bus frequency can reasonably approximate rotor speed.
- The proposed method achieves estimation accuracy comparable to conventional SI-based approaches without requiring model-order selection, rotor-speed reconstruction, or RoCoF computation. This demonstrates that a simplified identification structure can deliver high-quality performance with reduced computational overhead.
- The proposed method shows high estimation performance for the Kundur two-area system, the IEEE Australian simplified 14-generator system, and the IEEE 39-bus system. Its performance remains consistent across these scenarios despite a common band-pass frequency range and a fixed first-order identification model.

This paper is organized as follows. Section 2 presents the system modeling framework for inertia estimation, while Section 3 describes the proposed band-pass filtering and SI approach. Section 4 evaluates the performance through simulations on benchmark systems, and Section 5 concludes the paper.

2. System Model for Inertia Estimation

This section establishes the theoretical foundation for the proposed inertia estimation method by presenting the swing equation of SGs, analyzing the low-frequency dynamics of governor–turbine (GT) systems, and clarifying the discrepancy between rotor speed and PMU frequency. These models provide the rationale for applying band-pass filtering and enable the formulation of a simplified first-order system for inertia estimation.

2.1. Swing Equation

The swing equation describes the dynamic relationship between rotor speed and power in SGs. Including damping effects, the swing equation [1] is expressed as

$$2H\frac{d\omega_r}{dt} = P_m - P_e - D(\omega_r - \omega_0) \tag{1}$$

where P_m and P_e denote mechanical and electrical power in per unit, respectively, and ω_r is the rotor rated angular velocity in per unit. Also, H and D are the generator inertia constant and the damping coefficient, respectively. Assuming small perturbations, the swing equation can be expressed as a small-signal model around the steady-state equilibrium point [1]. That is

$$2H\frac{d\Delta\omega_r}{dt} = \Delta P_m - \Delta P_e - D\Delta\omega_r \tag{2}$$

where $\Delta\omega_r = \omega_r - \omega_{r_0}$ represents the deviation from the steady-state angular velocity in p.u. The terms $\Delta P_m = P_m - P_{m_0}$ and $\Delta P_e = P_e - P_{e_0}$ respectively represent the deviations

from the steady-state mechanical power and electrical power in p.u. The steady-state equilibrium points are denoted by ω_{r_0}, P_{m_0}, and P_{e_0}.

2.2. Low-Frequency Dynamics of GT Systems

The GT system regulates the P_m delivered to a synchronous generator. For analytical purposes, the GT dynamics can be approximated by an equivalent first-order model. In this representation, P_m is regarded as the state variable that characterizes the GT response, while the parameter T_a denotes the aggregate time constant of the governor and turbine. The state equation of the first-order GT model is expressed as

$$\dot{P}_m = \frac{1}{T_a}\left(P_r - \frac{1}{R_d}\Delta\omega_r - P_m\right), \tag{3}$$

where P_r and R_d are the reference power and the speed regulation constant, respectively. By converting this state-space model into a transfer function, the relation between the rotor speed deviation $\Delta\omega_r$ and the mechanical power variation ΔP_m is obtained as

$$G(s) = \frac{-1/R_d}{T_a s + 1}. \tag{4}$$

This transfer function indicates that the GT system behaves as a low-pass filter. Consequently, P_m is insensitive to high-frequency components and mainly reflects low-frequency dynamics. Thus, P_m can be interpreted as a variable dominated by low-frequency behavior.

2.3. Difference Between Rotor Speed and PMU Frequency

The electrical frequency measured at the generator terminal bus is not identical to the rotor speed. This deviation is represented by the frequency-divider relationship [22]. That is,

$$\Delta\omega_r = \Delta f - x_{\text{eq}}\frac{dP_e}{dt}, \tag{5}$$

where x_{eq} and Δf (in p.u.) denote the generator's equivalent internal reactance, and the terminal-bus frequency deviation measured by PMUs, respectively. As indicated in (5), the magnitude of the deviation between the rotor speed and the terminal frequency depends on the value of x_{eq} and the rate of power variation. According to (5), the mismatch between Δf and $\Delta\omega_r$ increases as the magnitude of $|dP_e/dt|$ becomes larger. This difference becomes more pronounced in higher-frequency regions, since differentiation in the time domain corresponds to multiplication by $j\omega$ in the frequency domain. Such behavior provides one design rationale for the band-pass filter described in Section 3, indicating that the analysis should be confined to a frequency range where Δf can reliably approximate $\Delta\omega_r$.

3. Inertia Estimation by Band-Pass Filtering of PMU Data

This section presents the proposed inertia estimation framework that integrates band-pass filtering with SI. Figure 1 shows the overall flow of the proposed method. After preprocessing the PMU measurement data (Section 3.1), appropriate cut-off frequencies are introduced to suppress the influence of governor–turbine dynamics and mitigate the discrepancy between rotor speed and PMU frequency (Section 3.2). Then, the filtered swing equation is reformulated into a first-order representation, enabling direct estimation of the inertia constant through SI. The AutoRegressive Moving Average with eXogenous input (ARMAX)-based identification approach is described in detail, along with its parameter mapping to the swing equation (Section 3.3).

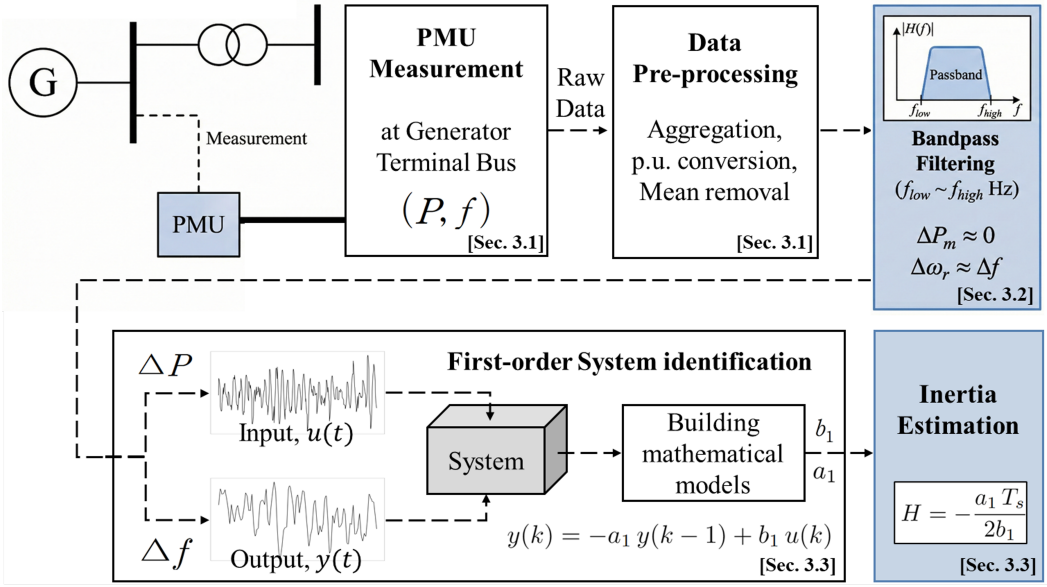

Figure 1. The overall flow of the proposed method.

3.1. Preprocessing of PMU Measurements

In practice, PMUs can acquire active power P and frequency f at each generator terminal bus. The PMU frequency is the electrical frequency at the terminal, which may differ from the rotor speed at high frequencies due to the internal reactance of the generator. The regional active power is obtained by summing the active power of all generators in the region. The regional frequency is calculated as a weighted average of the measured generator bus frequencies. In [11], the weights are often chosen in relation to the generator inertia, for example, by using the inverse of the variance of each bus frequency. The resulting regional frequency serves as a practical approximation of the center-of-inertia frequency, which cannot be measured directly. The aggregated P and f signals are then converted into per-unit values using the regional base power and the nominal frequency. Their mean values are removed to isolate dynamic variations and measurement noise.

3.2. Cut-Off Frequency of Band-Pass Filter

The proposed method critically depends on the proper selection of the band-pass filter cut-off frequencies. The filter ensures that the PMU-measured active power and frequency signals satisfy two key conditions for simplifying the swing equation: (i) the P_m can be neglected by removing slow governor–turbine dynamics, and (ii) the discrepancy between the terminal bus frequency and the rotor speed is mitigated by attenuating high-frequency components. To meet these conditions, two cut-off frequencies are introduced: low cut-off frequency f_{low} and high cut-off frequency f_{high}.

3.2.1. Low Cut-Off Frequency to Neglect GT Systems

For inertia estimation, an appropriate treatment of the influence of P_m is required because P_m cannot be directly measured by PMUs. In studies based on ringdown data, short-term transient variations of power are analyzed, which allows ΔP_m to be approximated as zero and removed. However, when ambient data obtained under quasi-steady state conditions are used, the direct assumption of $\Delta P_m = 0$ is not appropriate and may result in errors in the inertia estimation.

To address this issue, several prior studies [11,14] have proposed methods that explicitly model the transfer function of the GT system to incorporate its dynamics or apply

high-order identification approaches. However, these methods lead to an increase in model order and result in more complex identification procedures.

This study proposes a simpler alternative. Because the GT system responds slowly to changes (acting as a low-pass filter), ΔP_m variations are concentrated in the low-frequency range. Above a certain threshold frequency, the magnitude of ΔP_m rapidly decreases and converges to nearly zero. Hence, this threshold is defined as the low cut-off frequency f_{low}, and by removing frequency components below f_{low}, the approximation $\Delta P_m \approx 0$ becomes valid. This approach eliminates the need to explicitly model the GT dynamics, thereby reducing model complexity and enabling first-order SI with improved computational efficiency.

The method for determining the value of f_{low} is explained as follows. The ΔP_m follows the ΔP_e through the governor feedback loop. In the time domain, ΔP_m responds with delay and damping but ultimately tracks the changes in ΔP_e, which restores the power balance. In the frequency domain, the spectra of ΔP_m and ΔP_e are similar in the low-frequency range. Above a certain frequency, the governor dynamics restrict the response of ΔP_m and its contribution becomes negligible.

This property enables the identification of a threshold frequency by applying FFT to the measurable ΔP_e signal obtained from PMUs. The frequency at which the influence of ΔP_m diminishes is defined as f_{low}. Previous studies have shown that the dynamics of ΔP_m are concentrated below 0.1–0.2 Hz [26,27]. In practice, however, filters such as the Butterworth design do not provide an ideal cut-off response. They have a transition band around the cut-off point, which allows residual low-frequency components to remain. To suppress the effect of ΔP_m below 0.2 Hz, a slightly higher cut-off frequency is required. Therefore, this study adopts an empirical approach to determine f_{low}, and evaluates the robustness of the selected threshold under different system configurations. Note that from an engineering perspective, f_{low} can be practically selected by inspecting the spectral density of the measured ΔP_e signal and identifying the frequency above which the low-frequency components associated with GT dynamics rapidly decay.

3.2.2. High Cut-Off Frequency to Approximate Rotor Speed

The rotor speed deviation $\Delta\omega_r$ in the swing equation cannot be measured by PMUs. The bus frequency deviation Δf is, therefore, used as an approximation. In the low-frequency range, the two signals show similar behavior. At higher frequencies, the effect of the generator's internal reactance and local electromagnetic phenomena introduces differences. These differences can degrade inertia estimation. A restriction of the frequency range is therefore required.

To achieve this goal, a high cut-off frequency f_{high} is defined. The selection of f_{high} takes into account the low-frequency behavior of ΔP_m, the bandwidth of PMU measurements, and the need to attenuate noise. Previous research has reported that limiting the signal to the low-frequency band improves the reliability of inertia estimation [23]. In addition, the inter-area oscillations are typically observed below 1 Hz. Based on these considerations, this work adopts $f_{\text{high}} = 1.0$ Hz as a practical upper bound for the band-pass filtering stage.

3.3. System Identification Model for Inertia Estimation

As established in Section 3.2, ΔP_m can be neglected, and $\Delta\omega_r$ can be approximated by Δf. These approximations reduce the swing equation to a form that can be directly modeled using SI. In this work, the ARMAX model is employed for inertia estimation. The ARMAX framework is particularly suitable for this task because it represents both

the deterministic input–output dynamics and the stochastic disturbances inherent in PMU measurements, providing robustness when applied to ambient data.

In discrete time, a first-order ARMAX model is expressed as

$$y(k) = -a_1\, y(k-1) + b_1\, u(k-1) + c_1\, e(k-1) + e(k), \tag{6}$$

where $u(k)$, $y(k)$, and $e(k)$ denote the system input and the measured output, and a zero-mean white noise sequence, respectively. The coefficients a_1, b_1, and c_1 quantify the influence of past outputs, inputs, and disturbances, respectively. Parameter estimation is typically initiated by identifying a preliminary AutoRegressive model with eXogenous inputs (ARX), which provides initial parameter values without incorporating noise dynamics. These values are then iteratively refined using optimization-based methods such as the Maximum Likelihood Estimation (MLE) or the Prediction Error Method (PEM), which explicitly account for the noise term $e(k)$ in Equation (6). Finally, model validation is carried out by checking that the residual sequence behaves like white noise.

Once SI is completed in Equation (6), the noise terms are neglected, resulting in the simplified ARX representation. It is given as

$$y(k) = -a_1\, y(k-1) + b_1\, u(k), \tag{7}$$

where the input is $u(k) = \Delta P(k)$, and the output is $y(k) = \Delta f(k)$. Although this ARX form is not used in the actual estimation, it clarifies the direct relationship between the model coefficients and the physical parameters of the swing equation.

The swing equation under the approximations $\Delta P_m \approx 0$, $\Delta P_e \approx \Delta P$, and $\Delta\omega_r \approx \Delta f$ is given as

$$2H\,\frac{d\Delta f}{dt} = \Delta P - D\,\Delta f. \tag{8}$$

The derivative is discretized using a backward-difference operator with sampling interval T_s. That is

$$\frac{d\Delta f}{dt} \approx \frac{\Delta f(k) - \Delta f(k-1)}{T_s}. \tag{9}$$

Substituting this expression into the swing equation gives

$$2H\,\frac{\Delta f(k) - \Delta f(k-1)}{T_s} = \Delta P(k) - D\,\Delta f(k), \tag{10}$$

which can be rearranged as

$$\Delta f(k) = \left(\frac{2H}{2H + D\,T_s}\right)\Delta f(k-1) + \left(\frac{T_s}{2H + D\,T_s}\right)\Delta P(k). \tag{11}$$

This expression has the same structure as the ARX model, which allows the ARMAX coefficients to be directly linked with the swing equation parameters. The coefficients are respectively identified as

$$a_1 = -\frac{2H}{2H + D\,T_s}, \qquad b_1 = \frac{T_s}{2H + D\,T_s}, \tag{12}$$

Taking the ratio of a_1 and b_1 in (12) yields

$$\frac{a_1}{b_1} = \frac{-\frac{2H}{2H+DT_s}}{\frac{T_s}{2H+DT_s}} = -\frac{2H}{T_s}, \tag{13}$$

from which the inertia constant is obtained as

$$H = -\frac{a_1 T_s}{2 b_1}. \tag{14}$$

In summary, the approximations introduced in Section 3.2 enable the swing equation to be reformulated into a first-order SI model. The ARMAX approach is employed to identify the coefficients from ambient data, while the simplified ARX model serves as a conceptual tool for parameter mapping. The backward-difference operator improves stability and estimation accuracy compared to the forward scheme. Although ARMAX is adopted in this study, alternative SI approaches such as regression-based methods or subspace-based state-space identification, e.g., N4SID, can also be used to derive the first-order transfer function and compute the inertia constant. The selection of an SI method should therefore balance model fidelity, robustness against noise, and computational efficiency.

4. Case Study

The proposed method was evaluated using three benchmark systems: the Kundur two-area system, the IEEE Australian simplified 14-generator system, and the IEEE 39-bus system. Note that these systems are widely adopted synthetic benchmark networks in the literature for validating electromechanical dynamics and inertia-related behavior in power systems [11,14,17,28,29]. Detailed descriptions of each system are provided in Sections 4.2–4.4.

4.1. Simulation Settings

To model load variations under ambient operating conditions, white Gaussian noise with zero mean and a standard deviation of 1% of each load's base power was applied, which is consistent with values reported in previous studies [14,30]. Reactive power Q was modeled in the same manner. Frequency f and active power P were measured at the generator terminal buses through PMUs with a reporting interval of $T_s = 1/60$ s, while the mechanical input power P_m was directly obtained from the SimPowerSystems (SPS) discrete-time model in MATLAB/Simulink. To further reflect realistic measurement conditions, additive white Gaussian noise with a signal-to-noise ratio of 40 dB was added to the signals [31].

Each simulation was conducted for 14 min and 30 s. To eliminate the influence of initial transients, the first 30 s were discarded, and the subsequent 14 min of data were used for inertia estimation. The simulations were performed in MATLAB/Simulink R2022b on a personal computer equipped with an Intel(R) Core(TM) i7-13700K 13th Gen processor (3.40 GHz) and 32 GB RAM.

In this study, inertia is estimated using data windows on the order of a few minutes with a sliding update interval of 1 s. The computation time per update is approximately 0.1 s, which is shorter than the refresh interval. These settings indicate that the proposed method can provide near real-time updates and accurate inertia estimation for regional inertia monitoring.

To quantitatively assess the estimation performance under the above settings, the following error metric was used:

$$\text{Error (\%)} = \frac{H_{\text{real}} - H_{\text{est}}}{H_{\text{real}}} \times 100. \tag{15}$$

4.2. Kundur Two-Area System

This system consists of four SGs, eleven buses, two loads, and two 230 kV transmission lines, each 220 km in length, connecting the two areas. The rated frequency and base power

of the system are 60 Hz and 1000 MW, respectively. Each area is equipped with two round-rotor SGs rated at 20 kV/900 MVA. All machines share identical electrical parameters, with the only difference being their inertia constants. All generators are modeled as thermal power plants equipped with identical governors and high-speed static exciters with a gain of 200. The overall configuration of the Kundur two-area system is illustrated in Figure 2. The composition of each area and the corresponding generator inertia constants are summarized in Table 1. Detailed parameter values are in [1].

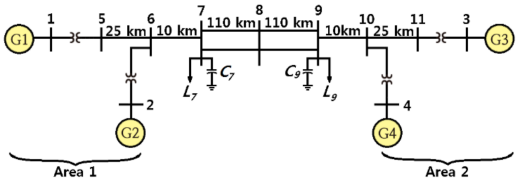

Figure 2. The single-line diagram of the Kundur two area system.

Table 1. Kundur Two-Area System Composition and Inertia Constants.

	Generator	H (s)	H_{area} (s)
Area 1	G1	6.500	13.00
	G2	6.500	
Area 2	G3	6.175	12.35
	G4	6.175	

In this study, the spectral density function (SDF) was employed to analyze P_m and P_e in the frequency domain. A direct inspection in the time domain does not clearly reveal the spectral characteristics of the signals, whereas frequency-domain analysis enables a more effective interpretation of the underlying dynamics. The SDF is typically obtained from periodograms, defined as the squared magnitude of the discrete Fourier transform. However, a single periodogram suffers from severe bias and large variance, which makes it unsuitable for reliable analysis [32]. To address this issue, Welch's method was adopted in this work. Specifically, the data were divided into partially overlapped segments, and each segment was windowed with a Hanning function to reduce boundary effects. The periodograms computed from each segment were then averaged, and zero-padding was applied to improve frequency resolution. The detailed parameters for this procedure are provided in [30]. This procedure yields an averaged SDF with reduced variance and improved statistical stability, thereby enabling a reliable spectral comparison between P_m and P_e.

Figure 3 shows the result of spectral characteristics. The spectral magnitude of P_m converges to nearly zero above approximately 0.2 Hz. In addition, ΔP_m and ΔP_e exhibit similar frequency-domain characteristics in the low-frequency range. These results indicate that, although TSOs cannot directly measure P_m under typical operating conditions, the frequency-domain analysis of P_e provides information that reflects the dynamic characteristics of P_m.

4.2.1. Impact of Neglecting P_m

Figure 4 shows the inertia estimation errors. To investigate the effect of the lower cutoff frequency f_{low}, the inertia estimation performance was compared for $f_{\text{low}} = 0$, 0.15, 0.35, and 0.55. The violin plots illustrate the distribution of the estimation error, where the internal horizontal lines denote the quartiles and the median, and the marker indicates the sample mean. All configurations employed third-order Butterworth filters with a 1 Hz high cutoff frequency and a 120 s estimation window. A total of 14 min of data were processed

with a 1 s sampling interval, which resulted in $(14-2) \times 60$ estimation samples for each band-pass filter configuration.

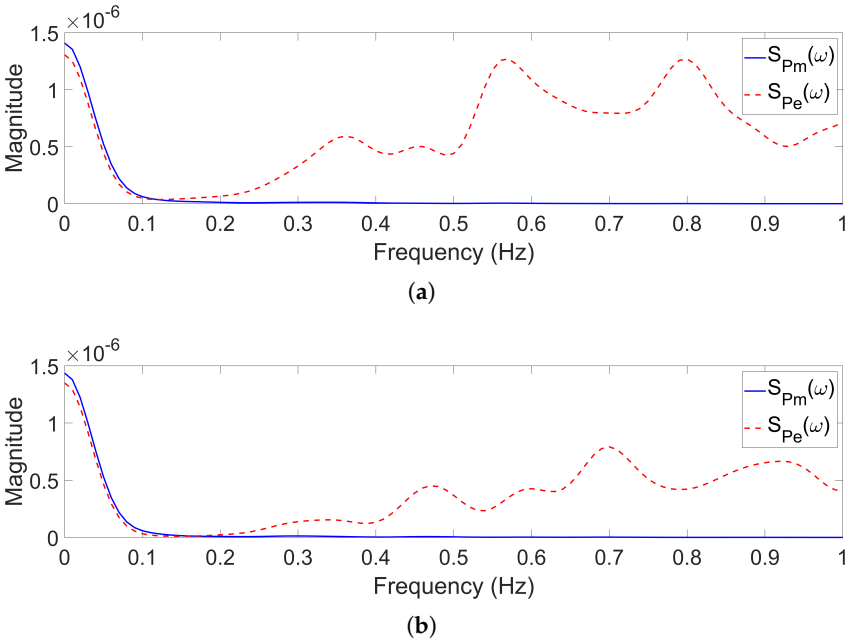

Figure 3. SDFs $S_{P_m}(\omega)$ and $S_{P_e}(\omega)$. (**a**) SDF of Area1; (**b**) SDF of Area2.

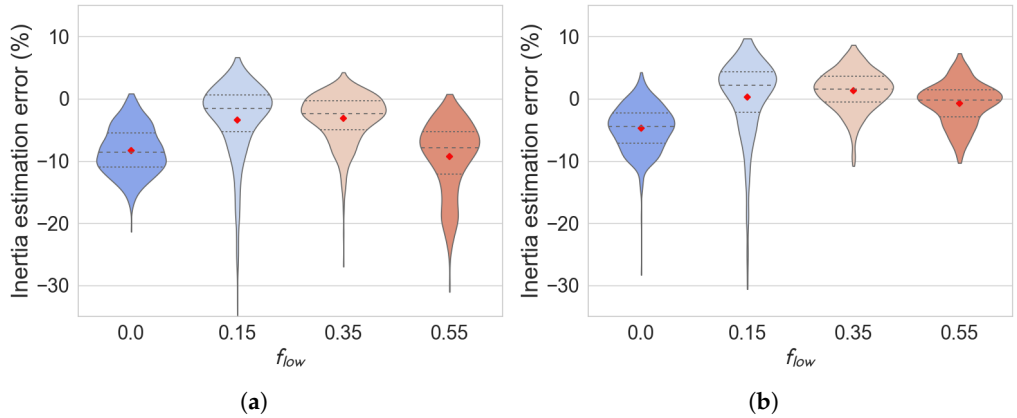

Figure 4. Violin plot of inertia estimation error versus f_{low} for each area. (**a**) Area1; (**b**) Area2.

When $f_{\text{low}} = 0$, the filter acts as a low-pass filter that allows the entire P_m component to pass through. Consequently, low-frequency disturbances and slow variations in P_m biased the estimation results, yielding mean errors of approximately -8.3% in Area 1 and -4.7% in Area 2. As f_{low} increased, the effect of slow power variations became less significant because low-frequency components were progressively attenuated. At $f_{\text{low}} = 0.35$, the mean estimation errors improved to about -3.1% in Area 1 and 1.3% in Area 2, demonstrating a well-balanced trade-off between bias reduction and variance stability. These findings suggest that the chosen frequency range mitigates the low-frequency influence of P_m, leading to more accurate and stable inertia estimation results.

However, when f_{low} was increased further to 0.55 Hz, the mean error in Area 1 decreased again to approximately -9.3%, implying that excessive filtering removed part of the useful inertial response and led to degraded estimation performance. Therefore, $f_{\text{low}} = 0.35$ Hz is identified as the most suitable lower cutoff frequency, providing a stable balance between bias reduction and dynamic information preservation. In the subse-

quent analysis, the proposed band-pass filter is configured with fixed cutoff frequencies of 0.35–1 Hz.

This selection was guided by a parameter sweep. Before producing the results in Figure 4, f_{low} was varied from 0.2 to 0.5 Hz in steps of 0.05 Hz. Among these values, 0.35 Hz produced stable behavior and was chosen as a representative setting. This does not imply that 0.35 Hz is the global optimum. Frequencies between 0.15 Hz and 0.35 Hz may result in similar or improved performance. For this reason, Figure 4 includes 0.35 Hz along with nearby candidates at 0.15 Hz and 0.55 Hz, together with the case of $f_{\text{low}} = 0$, to show the overall trend with respect to the lower cutoff frequency.

When f_{low} increased to 0.55 Hz, the mean error in Area 1 decreased again to approximately −9.3%. This behavior indicates that excessive filtering removed part of the useful inertial response and degraded the estimation performance. Based on these observations, the subsequent analysis adopts a band-pass filter with a lower cutoff frequency of 0.35 Hz and an upper cutoff frequency of 1 Hz.

4.2.2. Effect of Filter Order

The objective of the proposed band-pass filter is to effectively suppress the influence of P_m while preserving the information contained in P_e. To achieve this goal, not only the cutoff frequency but also the choice of filter structure is critical. In this study, two representative IIR designs, the Butterworth and Chebyshev Type II filters, were applied, and their orders were varied from two to five.

Table 2 shows the estimation results by area, filter type, and order. The Butterworth filter is characterized by a maximally flat passband, which is advantageous for preserving the passband components of P_e. However, its attenuation slope is relatively gradual for a given order, making it less effective in suppressing P_m components near the cutoff frequency. In contrast, the Chebyshev Type II filter provides a steeper stopband attenuation, which improves the rejection of P_m components, though at the expense of larger phase distortion and group delay variations near the passband edge.

Table 2. Comparison of error mean and standard deviation (Std.) by area, filter type, and order.

Area	Order	Mean Error (%)		Std. (%)	
		Butterworth	**Chebyshev II**	**Butterworth**	**Chebyshev II**
1	2	−3.259	0.833	3.835	6.657
	3	−3.149	0.563	3.902	4.160
	4	−3.141	−0.325	3.768	3.657
	5	−2.767	−3.607	3.895	3.822
2	2	1.281	6.578	3.221	5.026
	3	1.296	4.633	3.266	3.346
	4	1.186	3.913	3.365	3.366
	5	1.346	2.027	3.468	3.626

As shown in Table 2, the absolute values of the mean errors were generally within 5% for both filters, except for Area 2 with the second-order Chebyshev Type II, which reached 6.578%. In Area 1, the fourth-order Chebyshev Type II achieved the most stable performance with a mean error of −0.325% and a standard deviation of 3.657%, outperforming the fourth-order Butterworth (mean error of −3.141%, standard deviation of 3.768%) in terms of both bias and variance. In Area 2, the Chebyshev Type II filter showed a clear improvement as the order increased: the mean error decreased from 6.578% at second order to 2.027% at fifth order, while the standard deviation was reduced from 5.026% to 3.626%.

Figure 3 provides partial support for this interpretation. Compared to Area 2, Area 1 appears to exhibit a larger relative energy of P_m with respect to P_e near the cutoff frequency of 0.35 Hz. Under this condition, a sharper attenuation slope may help suppress residual P_m while preserving P_e, which could be related to the superior performance of the Chebyshev Type II filter relative to the Butterworth filter. In contrast, Area 2 shows a smaller relative energy of P_e in the 0.2–0.4 Hz band, which may reduce the benefit of a steeper roll-off. As a result, the Chebyshev Type II filters did not necessarily outperform the Butterworth filters in that area.

4.2.3. Effect of Window Size Estimation

Inertia estimation requires both accuracy and real-time performance. The window length must therefore balance bias and variance. The window length was varied from 60 to 240 s in 10-s increments during the simulation. Four representative window sizes of 60, 120, 180, and 240 s were selected from the full set of results and are presented in Table 3. These values illustrate how the estimation performance changes as the window becomes longer.

Table 3. Comparison of error mean and standard deviation by area and window size.

Area	Window	Mean Error (%)	Std. (%)
1	60	−2.034	6.664
	120	−0.325	3.657
	180	0.094	2.538
	240	0.254	2.031
2	60	1.660	7.331
	120	3.913	3.366
	180	4.711	2.169
	240	5.143	1.739

In Area 1, the mean error decreased from −2.034% to 0.254% as the window size increased, and the standard deviation was reduced from 6.664% to 2.031%. This indicates that longer windows lower the variance through noise averaging. Even with a 60 s window, the mean error was acceptable, but the variance remained high. In Area 2, the mean error increased from 1.660% to 5.143% with larger windows, while the standard deviation decreased from 7.331% to 1.739%. Thus, shorter windows yield smaller bias but larger variance, whereas longer windows reduce variance at the cost of increased bias.

Overall, the Chebyshev Type II filter showed consistent variance reduction with longer windows, and in Area 1, bias also improved. These results highlight the need to balance bias and variance when selecting the window size. With a 120 s window, the mean error was −0.325% with a standard deviation of 3.657% in Area 1, and 3.913% and 3.366% in Area 2, respectively. Hence, the 120-s window is adopted as a representative choice based on its performance in the Kundur two area system. This selection supports consistent evaluation across other systems and does not imply that the window is a global optimal.

4.3. IEEE Australian Simplified 14-Generator System

This system is a benchmark model that was developed by simplifying the southern and eastern Australian power systems. It consists of 59 buses, 14 SGs, and 29 loads, and the rated frequency is 50Hz. Except for Generator 1 in Area 1, all remaining 13 generators are equipped with turbine and governor models based on common parameter sets. The overall configuration of the IEEE Australian Simplified 14-Generator System is illustrated in Figure 5. Table 4 shows the composition of each area and the corresponding generator inertia constants. Detailed parameter values are in [33].

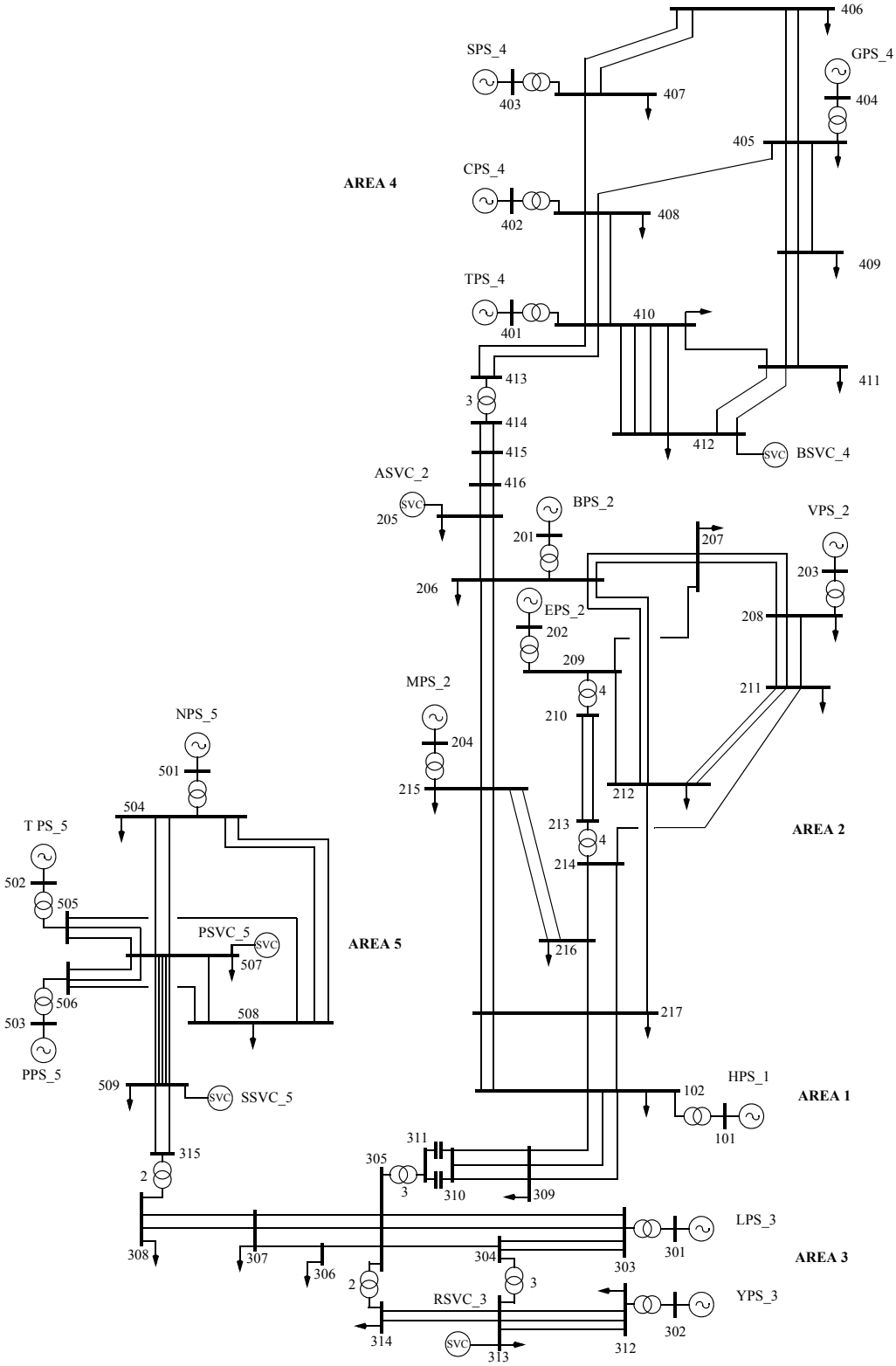

Figure 5. Single-line diagram of the IEEE Australian Simplified 14-Generator System, reproduced with the permission of the authors of [33].

https://doi.org/10.3390/en19020424

Table 4. System Composition and Inertia Constants by Area.

	Generator	H (s)	H_{area} (s)
Area 1	G1	3.6	3.6
Area 2	G2	3.2	11.8
	G3	2.8	
	G4	2.6	
Area 3	G6	2.8	6.3
	G7	3.5	
Area 4	G8	2.6	12.2
	G9	3.0	
	G10	2.6	
	G11	4.0	
Area 5	G12	3.5	15.0
	G13	4.0	
	G14	7.5	

The system is divided into five areas. Area 1 contains a single generator that represents an aggregated unit formed by combining multiple power stations and nearby resources into one equivalent machine. As a result, Area 1 functions as a special modeling region rather than a typical multi-generator area. Consequently, Area 1 is excluded from the analysis, and inertia estimation is performed only for Areas 2–5. Among Areas 2–5, Figure 6 shows the SDFs of P_m and P_e for Areas 2 and 5. It is because the spectral characteristics of Areas 3 and 4 are similar to those of Area 2. The inertia estimation results presented below are obtained using a fourth-order Chebyshev Type II filter with a 120-s window, selected based on the analysis in Section 4.2.

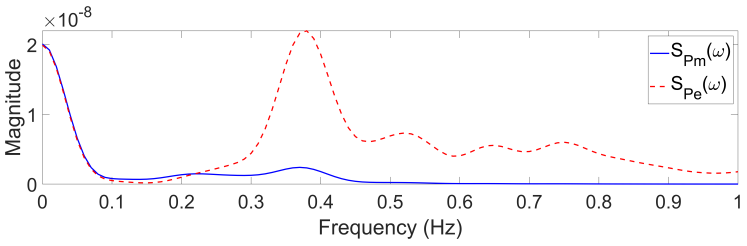

(**a**)

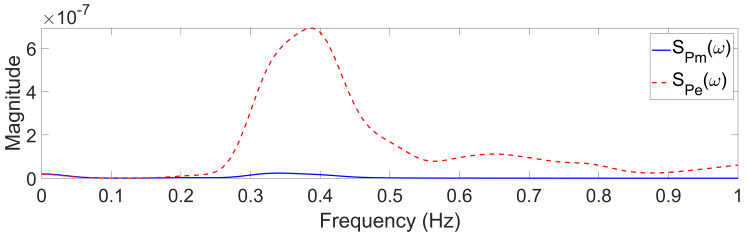

(**b**)

Figure 6. SDFs $S_{P_m}(\omega)$ and $S_{P_e}(\omega)$. (**a**) SDF of Area2; (**b**) SDF of Area5.

4.3.1. Impact of Neglecting P_m

In the Australian system, the effect of applying Low-pass and Band-pass filters on inertia estimation was analyzed in the same manner as for the Kundur system. These estimation results are plotted in Figure 7. In Areas 2–4, the application of the Band-pass filter shifted the mean error distribution closer to zero and reduced the variance. This indicates that the Band-pass filter contributed to improving both accuracy and stability by suppressing the influence of P_m.

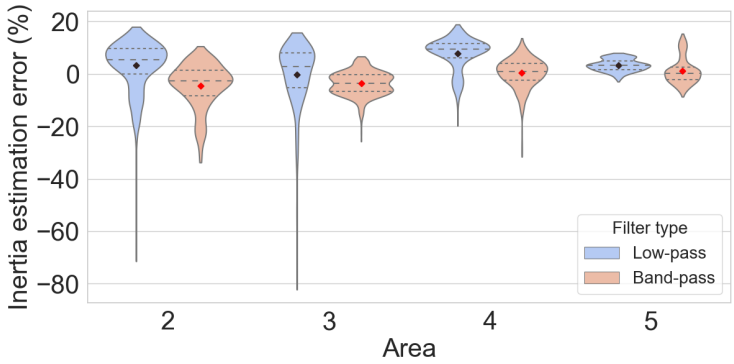

Figure 7. Band-pass filter effect.

In Area 5, the results show that the variance with the Low-pass filter was smaller, and the performance of the Low-pass filter visually appeared comparable to that of the band-pass filter. This behavior is also explained through the SDF analysis Figure 6. Unlike Areas 2, the SDF of Area 5 exhibited a y-axis scale of approximately 10^{-7}, about ten times larger than in the other areas, making the relative contribution of P_m less significant. Furthermore, the spectrum appeared relatively flat, and as a result, the application of the Band-pass filter did not show a clear difference compared with the Low-pass filter. Therefore, in Area 5, the variance results indicate that the performance difference between the two filters was not as evident as in the other areas.

4.3.2. Impact of Different Stochastic Load Models on Estimation Accuracy

This subsection examines the performance of the proposed estimator under several stochastic load representations. The analysis considers both Gaussian disturbances, as assumed in the previous section, and Ornstein–Uhlenbeck (OU) processes with different autocorrelation characteristics. The objective is to determine whether the estimator remains reliable when the statistical properties of the load variations differ from the nominal assumptions.

The OU process is a mean-reverting stochastic model commonly used to describe slow variations in aggregated loads. Its formulation follows established practices in stochastic load modeling [11,34,35]. This structure captures the temporal continuity and spectral trends typically observed in practical load fluctuations. The OU process exhibits a specific autocorrelation that describes how quickly the signal returns to its mean value. A larger autocorrelation corresponds to faster decaying fluctuations, whereas a smaller autocorrelation reflects slower load variations. Because these characteristics depend on the composition of the loads and the scale of the network, the OU representation provides a flexible means to model different disturbance patterns. Several autocorrelation conditions are therefore examined to assess the robustness of the proposed estimator.

Table 5 shows three disturbance scenarios. Scenario 1 introduces Gaussian noise with a standard deviation of 1%, consistent with the modeling assumption described earlier. Scenario 2 employs an OU process characterized by a 1% standard deviation and an autocorrelation of 0.5 Hz, which aligns with levels commonly observed in practical power systems. Scenario 3 maintains the same standard deviation but decreases the autocorrelation to 0.1 Hz to capture slower load variations.

A comparison of the results in Table 6 shows that the overall estimation performance remains stable across the three stochastic disturbance conditions. Although Scenario 3 exhibits larger mean errors and increased standard deviations compared to Scenario 2, this behavior is expected since a smaller autocorrelation reduces the variability of the OU process. As a result, less inertia-related information is present in the signal, which makes the estimation task more challenging. Despite this effect, none of the scenarios

show a significant degradation, indicating that the proposed method remains reliable even when the spectral properties of the load fluctuations differ. These findings suggest that the estimator can operate effectively under a wide range of load models with different autocorrelation characteristics.

Table 5. Stochastic Disturbance Scenarios.

Scenario	Std.	Autocorrelation
1 (Gaussian)	1%	–
2 (OU)	1%	0.5 Hz
3 (OU)	1%	0.1 Hz

Table 6. Estimation Results under Different Stochastic Load Models.

	Scenario 1		Scenario 2		Scenario 3	
	Mean Error (%)	Std. (%)	Mean Error (%)	Std. (%)	Mean Error (%)	Std. (%)
Area 2	−4.567	8.638	−3.953	9.581	5.411	10.454
Area 3	−3.671	4.623	1.930	8.633	4.896	8.437
Area 4	0.286	5.751	4.535	4.085	5.516	6.393
Area 5	1.045	4.990	1.607	2.506	2.775	6.041

4.4. IEEE 39-Bus System

The IEEE 39-bus system was also employed for validation. This system consists of 10 generators, 39 buses, and 19 loads, as illustrated in Figure 8. Its rated frequency is 60 Hz, and the base power is 1000 MW. Additional operating conditions and parameter modeling details are provided in [36]. The inertia constants of the generators under estimation are summarized in Table 7. To reduce computational effort, eight loads were selected based on their capacity, located at buses 3, 4, 8, 15, 20, 21, 27, and 39. The standard deviation of the active power variations was set to approximately 1.47% of each load's base power, which corresponds to roughly 1% of the total reference power. Reactive power Q was modeled in the same manner. For the IEEE 39-bus benchmark system, Area 1 is excluded for the same reasons discussed above, and the analysis is conducted on the remaining areas.

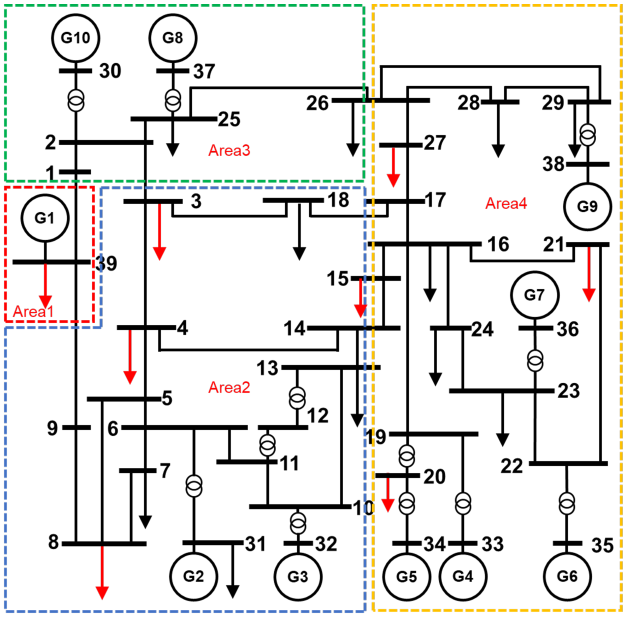

Figure 8. The single-line diagram of the IEEE 39-bus system.

Table 7. IEEE 39-Bus System Composition and Inertia Constants by Area.

	Generator	H (s)	H_{area} (s)
Area 1	G1	50.00	50.00
Area 2	G2	3.03	6.61
	G3	3.58	
Area 3	G8	2.43	6.63
	G10	4.20	
Area 4	G4	2.86	15.03
	G5	2.60	
	G6	3.48	
	G7	2.64	
	G9	3.45	

4.4.1. Impact of Neglecting P_m

In the IEEE 39-bus system, the influence of applying low-pass and band-pass filters on the proposed inertia estimation method was evaluated following the same procedure used for the Kundur and Australian systems. Figure 9 shows the results. Both filters provided stable estimation performance, and the band-pass filter led to a mean error distribution closer to zero with reduced variance. These outcomes are consistent with those observed in the previous test systems, indicating that the proposed approach maintains reliable performance across different network configurations.

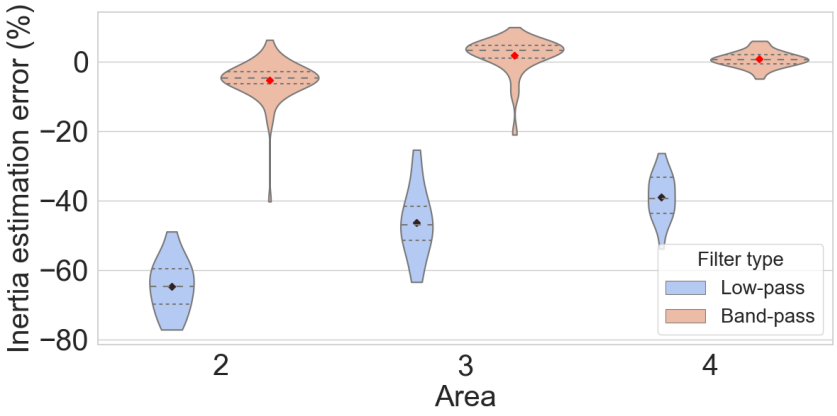

Figure 9. Band-pass filter effect.

4.4.2. Comparison with Existing System Identification Methods

This subsection compares the proposed approach with existing SI-based inertia estimation methods. The comparison focuses on how each method treats P_m, ω_r, and f, because these modeling choices determine the resulting system structure and identification procedure. In this section, two comparison schemes are considered. The former is SI with a second-order model [14], named Method I, which requires rotor-speed reconstruction from PMU measurements. The letter is N4SID with adaptation of a high-order model [11], named Method II, which requires model-order selection and RoCoF computation after SI. On the other hand, the proposed method does not require model-order selection, rotor-speed reconstruction, or RoCoF computation. Among the wide range of SI studies, this comparison considers methods that (i) utilize ambient measurements, (ii) estimate regional inertia from identical PMU locations, and (iii) adopt different model orders. The comparison is summarized in Table 8. In the table, shorter estimation windows indicate lower computational burden for online implementation.

Table 8. Comparison of SI-Based Inertia Estimation Methods.

Method	ω_r	P_m	Filter	Accuracy	Window
Method I [14]	$\hat{\omega}_r$	included in transfer function	2 Hz low-pass	1.5–3.5%	3–5 min
Method II [11]	$\approx f$	implicitly embedded	0.5 Hz low-pass	2–3.6%	4 min
Proposed	$\approx f$	≈ 0	0.35–1 Hz band-pass	0.5–4.5%	2 min

Method I employs a fixed second-order transfer function model in which the influence of P_m is explicitly incorporated. Method I reconstructs the rotor speed from PMU measurements because TSOs cannot directly access rotor-speed signals in practice. When a rotor-speed estimator is stably implemented, high-frequency components up to approximately 2 Hz can be utilized, allowing a broader frequency range than the 1 Hz band adopted in the proposed method. This provides an opportunity to exploit richer dynamic information. At the same time, rotor-speed estimation and high-bandwidth filtering introduce additional preprocessing steps, and their performance may depend on measurement quality and estimator design. This behavior is consistent with the spectral characteristics shown in Figure 10. The figure presents the SDFs of Generators 4 and 8 in the IEEE 39-bus system, where the rotor speed is compared with the terminal-bus frequency measured by the PMU. The two signals match in the low-frequency region but begin to diverge as the frequency increases, indicating that the effective use of high-frequency components depends on the accuracy of rotor-speed estimation. In this approach, SI aims to represent the overall electromechanical dynamics, including the effect of P_m, rather than focusing specifically on inertia-related behavior.

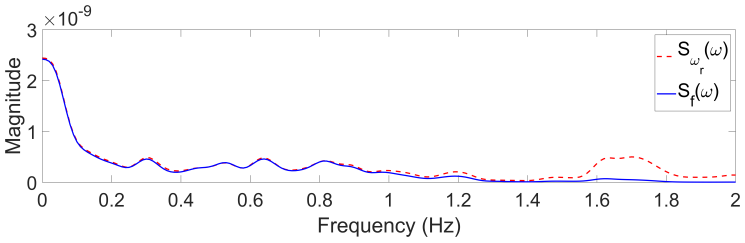

(**a**)

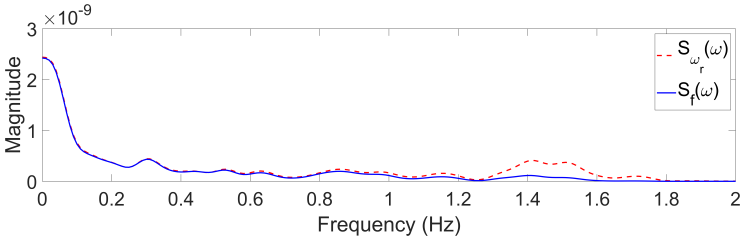

(**b**)

Figure 10. SDFs $S_{\omega_r}(\omega)$ and $S_f(\omega)$. (**a**) SDF of Generator 4; (**b**) SDF of Generator 8.

Method II adopts a multi-order modeling framework in which the system order is varied from $n = 2$ to $n = 10$, and the order that maximizes the fitting ratio is selected. This approach allows the model to represent a wide range of dynamic behaviors, which is valuable because real generator dynamics may not conform to simplified low-order structures. However, the order selection process requires dividing the data into estimation and validation sets, which increases the amount of data needed for reliable identification. The fitting ratio is also sensitive to measurement noise. Nevertheless, when sufficient data are available and the identified model is well validated, high estimation accuracy has been reported in prior studies. In addition, Method II estimates inertia by computing the RoCoF from model-based frequency variations after the transfer function has been identified. A

unit-step input is applied to the identified model to generate the step response, and the initial slope of the frequency deviation is used as RoCoF. The RoCoF calculation uses the 500 ms sample-by-sample sliding-window method introduced in [24]. Due to this structure, the accuracy of Method II depends on the reliability of RoCoF estimation. As a result, inertia estimation in this method relies on additional processing after SI, rather than being obtained directly from the identified model parameters.

The proposed method applies band-pass filtering to the measured P and f for constructing a first-order representation of the swing equation. Method I and Method II are also designed with consideration of practical measurement constraints in real power system operation. However, these methods address such constraints through explicit procedures such as ω_r reconstruction, RoCoF computation, or identification of higher-order electromechanical dynamics. In contrast, the proposed approach assumes that P_m and ω_r are not directly measurable and adopts band-pass filtering as a practical means to indirectly mitigate their influence using measurable signals only. The filtering process suppresses the low-frequency component associated with P_m, which allows P_m to be approximated as zero. Rotor-speed estimation and RoCoF calculation are not required, and no order-selection step is needed. These characteristics simplify the identification procedure and reduce computational burden, which is advantageous for real-time or online applications. A narrow band-pass filter is used to extract the inertia-related frequency components. This design supports stable estimation, although the selection of the filter band may cause variations in performance under different operating conditions.

The system order required for SI-based inertia estimation is closely related to the treatment of P_m. When P_m is explicitly represented, the GT dynamics introduce an additional low-frequency state and increase the effective system order. This motivates the use of second- or higher-order identification frameworks, as in Methods I and II. In contrast, when P_m is suppressed through band-pass filtering or approximated as zero within the selected frequency range, the swing equation reduces to a first-order model. This structure allows the proposed approach to operate with a low-order model without explicitly modeling governor dynamics.

The elimination of the order-selection step is a design choice that focuses on the dynamic behavior relevant to inertia estimation under ambient operating conditions. By fixing the model order to first order, the proposed method adopts a simplified SI structure that enables inertia estimation without explicitly modeling mechanical power variations or rotor-speed dynamics. Higher-order SI approaches represent more complex electromechanical dynamics by jointly modeling mechanical power and governor dynamics. This distinction reflects differences in the modeling scope addressed by each method. Accordingly, the proposed approach can be understood as an identification framework that is deliberately restricted to the objective of inertia estimation using only measurable signals.

Although the proposed framework primarily relies on low-frequency components, it can be extended to incorporate higher-frequency information when rotor-speed estimation is available. As shown in Figure 10, the terminal-bus frequency follows the rotor speed only within a limited low-frequency band, and the two signals begin to differ from each other as frequency increases. This behavior indicates that the usable frequency range is constrained by the accuracy of rotor-speed estimation. A reliable estimator enables higher-frequency dynamics to be preserved and incorporated into the identification process, providing additional flexibility in data utilization.

The three methods differ in their treatment of P_m, ω_r, and f, as well as in their filtering and order-selection procedures. These differences represent alternative modeling choices suited to different system and measurement conditions rather than indicators of superiority.

5. Conclusions

This paper presented a regional inertia estimation method in power systems using ambient PMU measurements. The approach applies band-pass filtering to suppress low-frequency governor–turbine dynamics and to mitigate high-frequency discrepancies between rotor speed and terminal-bus frequency. These filtering characteristics enable the swing equation to be represented by a first-order model, allowing the inertia constant to be identified without model-order selection, rotor-speed estimation, or RoCoF processing. The proposed method was validated using the Kundur two-area system, the IEEE Australian simplified 14-generator system, and the IEEE 39-bus system. Across all test cases, the method achieved regional inertia estimates within approximately ±5% error and maintained an overall accuracy level under different stochastic load representations and operating conditions. The estimator also provided reliable performance using short estimation intervals on the order of a few minutes, indicating its potential suitability for near real-time inertia monitoring.

Future work will focus on applying the proposed framework to real-world power system data and extending its applicability to large-scale networks with high penetration of converter-interfaced generators (CIGs). While CIGs can be modeled as a first-order dynamic system, the effectiveness of the proposed method in mixed-generation systems may be influenced by generator–converter interactions and the implementation of virtual inertia and grid-forming control. Although the first-order assumption remains structurally valid, low-frequency suppression may limit the observability of virtual inertia, which warrants further investigation. Investigating appropriate modeling strategies and frequency-band selection in mixed-generation environments will therefore be an important direction for future research. Furthermore, integrating regional inertia estimation into frequency stability assessment and control strategies will be an important direction for enhancing operational reliability in low-inertia systems.

Author Contributions: Conceptualization, K.-Y.L. and J.K.H.; Methodology, K.-Y.L. and J.K.H.; Software, K.-Y.L.; Validation, K.-Y.L. and S.-G.Y.; Investigation, K.-Y.L.; Writing—original draft, K.-Y.L.; Writing—review & editing, S.-G.Y. and J.K.H.; Visualization, K.-Y.L. and S.-G.Y.; Supervision, S.-G.Y. and J.K.H. All authors have read and agreed to the published version of the manuscript.

Funding: This work was supported in part by the National Research Foundation of Korea (NRF) grant funded by the Ministry of Science and ICT (MSIT) of the Republic of Korea (2022R1F1A1074838); and in part by the Korea Institute of Energy Technology Evaluation and Planning (KETEP) (No. RS-2024-00398166).

Data Availability Statement: The original contributions presented in this study are included in the article. Further inquiries can be directed to the corresponding authors.

Conflicts of Interest: The authors declare no conflict of interest.

References

1. Kundur, P. Power system stability. In *Power System Stability and Control*; CRC Press: Boca Raton, FL, USA, 2007; Volume 10.
2. Milano, F.; Dörfler, F.; Hug, G.; Hill, D.J.; Verbič, G. Foundations and challenges of low-inertia systems. In Proceedings of the 2018 Power Systems Computation Conference (PSCC), Dublin, Ireland, 11–15 June 2018; IEEE: New York, NY, USA, 2018; pp. 1–25.
3. National Grid ESO. Response and Reserve Roadmap. Available online: https://www.neso.energy/document/157791/download (accessed on 11 January 2026).
4. Ulbig, A.; Borsche, T.S.; Andersson, G. Impact of low rotational inertia on power system stability and operation. *IFAC Proc. Vol.* **2014**, *47*, 7290–7297. [CrossRef]
5. Caminiti, C.M.; Spiller, M.; Dimovski, A.; Barbieri, J.; Ragaini, E.; Merlo, M. Integrated adequacy and stability BESS sizing criteria for hybrid diesel–PV microgrids in developing countries. *Sustain. Energy Technol. Assess.* **2025**, *83*, 104541. [CrossRef]
6. Lavanya, L.; Swarup, K. Inertia monitoring in power systems: Critical features, challenges, and framework. *Renew. Sustain. Energy Rev.* **2024**, *190*, 114076.

7. Tan, B.; Zhao, J.; Netto, M.; Krishnan, V.; Terzija, V.; Zhang, Y. Power system inertia estimation: Review of methods and the impacts of converter-interfaced generations. *Int. J. Electr. Power Energy Syst.* **2022**, *134*, 107362. [CrossRef]
8. Follum, J.D.; Tuffner, F.K.; Dosiek, L.A.; Pierre, J.W. *Power System Oscillatory Behaviors: Sources, Characteristics, & Analyses*; Technical Report; Pacific Northwest National Laboratory (PNNL): Richland, WA, USA, 2017.
9. Rauniyar, M.; Berg, S.; Subedi, S.; Hansen, T.M.; Fourney, R.; Tonkoski, R.; Tamrakar, U. Evaluation of probing signals for implementing moving horizon inertia estimation in microgrids. In Proceedings of the 2020 52nd North American Power Symposium (NAPS), Tempe, AZ, USA, 11–13 April 2021; IEEE: New York, NY, USA, 2021; pp. 1–6.
10. Vanfretti, L.; Dosiek, L.; Pierre, J.W.; Trudnowski, D.; Chow, J.H.; García-Valle, R.; Aliyu, U. Application of ambient analysis techniques for the estimation of electromechanical oscillations from measured PMU data in four different power systems. *Eur. Trans. Electr. Power* **2011**, *21*, 1640–1656. [CrossRef]
11. Zeng, F.; Zhang, J.; Chen, G.; Wu, Z.; Huang, S.; Liang, Y. Online estimation of power system inertia constant under normal operating conditions. *IEEE Access* **2020**, *8*, 101426–101436. [CrossRef]
12. Hua, W.; Li, D.; Mi, Y. Power system inertia estimation during normal operation using adaptive ensemble empirical mode decomposition. *Electr. Power Syst. Res.* **2025**, *241*, 111305. [CrossRef]
13. Tuttelberg, K.; Kilter, J.; Wilson, D.; Uhlen, K. Estimation of power system inertia from ambient wide area measurements. *IEEE Trans. Power Syst.* **2018**, *33*, 7249–7257. [CrossRef]
14. Gotti, D.; Bizzarri, F.; Brambilla, A.; del Giudice, D.; Grillo, S.; Linaro, D.; Ledesma, P.; Amaris, H. Inertia estimation of a power system area based on iterative equation error system identification. *IEEE Trans. Power Syst.* **2024**, *39*, 6469–6481. [CrossRef]
15. Yang, D.; Wang, B.; Ma, J.; Chen, Z.; Cai, G.; Sun, Z.; Wang, L. Ambient-data-driven modal-identification-based approach to estimate the inertia of an interconnected power system. *IEEE Access* **2020**, *8*, 118799–118807. [CrossRef]
16. Kerdphol, T.; Watanabe, M.; Nishikawa, R.; Hayashi, Y.; Mitani, Y. Inertia estimation of the 60 Hz Japanese power system from synchrophasor measurements. *IEEE Trans. Power Syst.* **2022**, *38*, 753–766. [CrossRef]
17. Bizzarri, F.; del Giudice, D.; Grillo, S.; Linaro, D.; Brambilla, A.; Milano, F. Inertia estimation through covariance matrix. *IEEE Trans. Power Syst.* **2023**, *39*, 947–956. [CrossRef]
18. Linaro, D.; Bizzarri, F.; Del Giudice, D.; Pisani, C.; Giannuzzi, G.M.; Grillo, S.; Brambilla, A.M. Continuous estimation of power system inertia using convolutional neural networks. *Nat. Commun.* **2023**, *14*, 4440. [CrossRef]
19. Liu, K.; Xu, Y.; Gu, W.; Ge, J.; Lu, S.; Mili, L.; Shen, C. A Bayesian approach for online inertia estimation of synchronous and nonsynchronous generators. *IEEE Trans. Instrum. Meas.* **2024**, *73*, 1006012. [CrossRef]
20. Muhammed, A.O.; Isbeih, Y.J.; El Moursi, M.S.; Elbassioni, K. Artificial intelligence (ai) advanced techniques for real-time inertia estimation in renewable-based power systems. *IEEE Trans. Ind. Appl.* **2024**, *61*, 2604–2619. [CrossRef]
21. Tan, B.; Peng, J.; Gao, N.; Zhao, J.; Tan, J. Comparative Study of Data-driven Area Inertia Estimation Approaches on WECC Power Systems. In Proceedings of the 2024 IEEE Power & Energy Society General Meeting (PESGM), Seattle, WA, USA, 21–25 July 2024; IEEE: New York, NY, USA, 2024; pp. 1–5.
22. Milano, F.; Ortega, A. Frequency divider. *IEEE Trans. Power Syst.* **2016**, *32*, 1493–1501. [CrossRef]
23. Zhang, J.; Xu, H. Online identification of power system equivalent inertia constant. *IEEE Trans. Ind. Electron.* **2017**, *64*, 8098–8107. [CrossRef]
24. Ashton, P.M.; Saunders, C.S.; Taylor, G.A.; Carter, A.M.; Bradley, M.E. Inertia estimation of the GB power system using synchrophasor measurements. *IEEE Trans. Power Syst.* **2014**, *30*, 701–709. [CrossRef]
25. Hwang, J.K. Inertia Estimation of Synchronous Generators Using PMU Ambient Data in the Frequency Domain. In Proceedings of the 2024 9th Asia Conference on Power and Electrical Engineering (ACPEE), Shanghai, China, 11–13 April 2024; IEEE: New York, NY, USA, 2024; pp. 1716–1721.
26. Duong, D.T.; Uhlen, K.; Jansson, E.A. Estimation of hydro turbine-governor system's transfer function from PMU measurements. In Proceedings of the 2016 IEEE Power and Energy Society General Meeting (PESGM), Boston, MA, USA, 17–21 July 2016; IEEE: New York, NY, USA, 2016; pp. 1–5.
27. Hwang, J.K.; Yoon, S.-G.; Lee, K.Y. Comparison of the Accuracy of Generator Dynamic State Estimation Based on the Treatment of the Governor-Turbine Mechanical Power. *IEEE Access* **2024**, *12*, 105187–105200. [CrossRef]
28. Poudyal, A.; Tamrakar, U.; Trevizan, R.D.; Fourney, R.; Tonkoski, R.; Hansen, T.M. Multiarea inertia estimation using convolutional neural networks and federated learning. *IEEE Syst. J.* **2021**, *16*, 6401–6412. [CrossRef]
29. Markovic, U.; Stanojev, O.; Aristidou, P.; Vrettos, E.; Callaway, D.; Hug, G. Understanding small-signal stability of low-inertia systems. *IEEE Trans. Power Syst.* **2021**, *36*, 3997–4017. [CrossRef]
30. Hwang, J.K.; Seppänen, J. Frequency-domain system identification of a first order governor-turbine model from PMU ambient data. In Proceedings of the 2023 IEEE 32nd International Symposium on Industrial Electronics (ISIE), Helsinki, Finland, 19–21 June 2023; IEEE: New York, NY, USA, 2023; pp. 1–4.

31. Brown, M.; Biswal, M.; Brahma, S.; Ranade, S.J.; Cao, H. Characterizing and quantifying noise in PMU data. In Proceedings of the 2016 IEEE Power and Energy Society General Meeting (PESGM), Boston, MA, USA, 17–21 July 2016; IEEE: New York, NY, USA, 2016; pp. 1–5.
32. Welch, P. The use of fast Fourier transform for the estimation of power spectra: A method based on time averaging over short, modified periodograms. *IEEE Trans. Audio Electroacoust.* **2003**, *15*, 70–73. [CrossRef]
33. Gibbard, M.; Vowles, D. *Simplified 14-Generator Model of the South East Australian Power System*; The University of Adelaide, South Australia: Adelaide, Australia, 2014; Volume 18, pp. 1–38.
34. Gorbunov, A.; Peng, J.C.H.; Bialek, J.W.; Vorobev, P. Can center-of-inertia model be identified from ambient frequency measurements? *IEEE Trans. Power Syst.* **2022**, *37*, 2459–2462. [CrossRef]
35. Adeen, M.; Milano, F. On the impact of auto-correlation of stochastic processes on the transient behavior of power systems. *IEEE Trans. Power Syst.* **2021**, *36*, 4832–4835. [CrossRef]
36. Brunelle, P. 10-Machine New-England Power System IEEE Benchmark. MATLAB Central File Exchange. 2016. Available online: https://www.mathworks.com/matlabcentral/fileexchange/54771-10-machine-new-england-power-system-ieee-benchmark (accessed on 11 January 2026).

Disclaimer/Publisher's Note: The statements, opinions and data contained in all publications are solely those of the individual author(s) and contributor(s) and not of MDPI and/or the editor(s). MDPI and/or the editor(s) disclaim responsibility for any injury to people or property resulting from any ideas, methods, instructions or products referred to in the content.